

# Temporal and Spectral Manipulations of Correlated Photons

Sunil Mittal,<sup>1,2</sup> Venkata Vikram Orre,<sup>1,2</sup> Alessandro Restelli,<sup>1</sup> Reza Salem,<sup>3</sup> Elizabeth A. Goldschmidt,<sup>4,1</sup> and Mohammad Hafezi<sup>1,2</sup>

<sup>1</sup>*Joint Quantum Institute, NIST/University of Maryland, College Park, MD 20742, USA*

<sup>2</sup>*Department of Electrical and Computer Engineering, and IREAP, University of Maryland, College Park, MD 20742, USA*

<sup>3</sup>*PicoLuz, LLC, Jessup, MD 20794, USA*

<sup>4</sup>*U.S. Army Research Laboratory, Adelphi, MD 20783, USA*

A common challenge in quantum information processing with photons is the limited ability to manipulate and measure correlated states. An example is the inability to measure picosecond scale temporal correlations of a multi-photon state, given state-of-the-art detectors have a temporal resolution of about 100 ps. Here, we demonstrate temporal magnification of time-bin entangled two-photon states using a time-lens, and measure their temporal correlation function which is otherwise not accessible because of the limited temporal resolution of single photon detectors. Furthermore, we show that the time-lens maps temporal correlations of photons to frequency correlations and could be used to manipulate frequency-bin entangled photons. This demonstration opens a new avenue to manipulate and analyze spectral and temporal wavefunctions of many-photon states.

Photons entangled in spectral-temporal degrees of freedom are extremely advantageous for robust, long-distance entanglement distribution [1–4]. This characteristic feature has led to the development of a variety of techniques for spectral and temporal manipulations of single photons [5–11]. Recently, spectral compression and expansion of photons has gained widespread attention in order to efficiently interface wide-band sources of correlated photons with narrow-band nodes of a quantum network, for example, quantum dots and atomic systems [10, 12–14]. At the same time, temporal magnification of photons facilitates high-fidelity photonic measurements in quantum simulations [15–18]. For example, on-chip temporal boson-sampling and quantum walks [19–23] can have photonic wavepackets with temporal features shorter than the resolution of existing single photon detectors [24–26].

A versatile approach to spectrally compress and temporally magnify single photons is using time-lens techniques. A time-lens mimics a spatial lens by exploiting the space-time duality, for example, the paraxial diffraction of a light beam is dual to the temporal dispersion of a light pulse [27]. While time-lensing has been used widely in the past for temporal compression and expansion of classical light pulses [28–30], its use for single photons is very recent. Specifically, time-lens based techniques have demonstrated spectral manipulations of single photons [13, 14, 31] and also time-resolved detection of a photon arriving in two time-bins [32]. However, these demonstrations have only manipulated single photons. To engineer multi-photon states, it is crucial to also manipulate spectral and temporal correlations of photons.

In this work, we use an electro-optic phase modulator (EOM) based time-lens to magnify the two-photon temporal wavefunction associated with time-bin entangled photons while simultaneously preserving their quantum correlations. Our time-lens is designed to work in the telecom domain, using standard dense-wavelength division multiplexing (DWDM) components and it achieves a temporal magnification of 9.6(2)x. First, we use this magnification to resolve

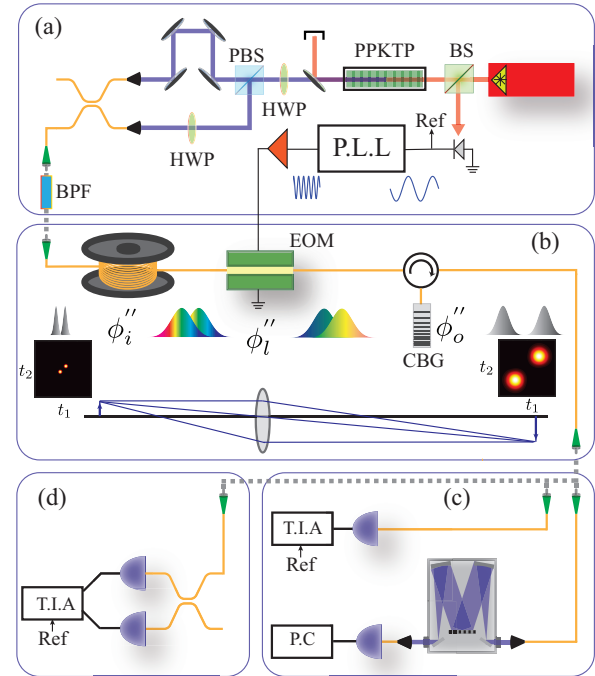


FIG. 1. (a), Time-bin entangled photons are generated using Type-II degenerate SPDC in a PPKTP crystal and a combination of a half-wave plate (HWP), a polarization beam-splitter (PBS) and a delay line. (b), A time-lens is implemented using 15 km of SMF-28 fiber, an electro-optic phase modulator (EOM) and a chirped Bragg grating (CBG) which emulates 150 km of SMF-28 fiber. (c), A SNSPD and a TIA were used for single-channel time-resolved detection of photons and a monochromator along with a SNSPD was used for spectral measurements. (d), For JTI measurements, the output of the time-lens was fed to a fused-fiber beamsplitter connected to two SNSPDs and a time-tagged coincidence counting electronics.

two photons with a delay much less than the resolution of our superconducting nanowire single photon detectors (SNSPDs). Then, we measure joint-temporal intensity (JTI) of the magnified two-photon wavefunction and distinguish correlations between bunched and anti-bunched time-bin entangled pho-

ton pairs, which is otherwise not measurable because of the limited resolution of SNSPDs. Finally, we show that the time-lens maps temporal correlations of incoming photons to frequency correlations of outgoing photons and can be used to manipulate frequency-bin entangled two-photon states [33].

Fig.1 illustrates a schematic of our time-lens setup. Following Ref. [27], analogous to a spatial lens creating a magnified image of an object, a time-lens has three components - input dispersion, the lens and output dispersion (see Fig.1(b)). A dispersive element with a group delay dispersion (GDD)  $\phi_i'' = \frac{d^2\phi_i(\omega)}{d\omega^2}$  is first used to spectrally chirp the input photon pulses. Here  $\omega$  is the angular frequency and  $\phi_i(\omega)$  is the frequency dependent phase-shift accumulated during propagation. This chromatic dispersion of an optical pulse is similar to the spatial diffraction of an optical beam while propagating from the object to the lens. Following initial dispersion, a nonlinear element - the time-lens - is used to introduce a phase-shift which varies quadratically with time. The function of time-lens is similar to that of a spatial lens which adds a spatially varying phase-shift to the diffracted beam. Here, we use an electro-optic phase modulator (EOM) as a time-lens. The required quadratic phase-shift is achieved by driving the EOM with a rf field of angular frequency  $\omega_m$  that imposes a phase-shift  $\phi_l(t) = -\frac{\pi V_m}{V_\pi} \cos(\omega_m t)$ , where  $V_m$  is the amplitude of the rf field and  $V_\pi$  is the voltage required to introduce a phase-shift  $\pi$ . Ensuring that  $\omega_m t \ll 1$  and that the two-photon wavepacket is locked to the phase of the rf drive allows the phase-shift to be approximated as  $\phi_l(t) = \frac{\pi V_m}{2V_\pi} \omega_m^2 t^2$  and the corresponding GDD is  $\phi_l'' = \frac{V_m}{\pi V_m \omega_m^2}$ . This quadratic time variation of phase also results in a linear frequency shift of the input photons, i.e., two photons incident on the time-lens with a delay  $\delta t_{\text{in}}$  between them are shifted in frequency by

$$\delta\nu = \frac{V_m}{V_\pi} \frac{\omega_m^2}{2} \delta t_{\text{in}}. \quad (1)$$

Therefore, the time-lens linearly maps any information contained in temporal degree of freedom of photons to the frequency domain. This is exactly analogous to the action of a spatial lens which Fourier transforms spatial information about an object to momentum domain. Finally, photons are subject to a large GDD at the output ( $\phi_o''$ ). This output GDD element acts as a frequency-to-time converter where the frequency shift  $\delta\nu$  leads to a differential delay  $2\pi\delta\nu\phi_o''$ . The total delay between the photons at the output of the lens is

$$\delta t_{\text{out}} = \delta t_{\text{in}} + \frac{\pi V_m}{V_\pi} \omega_m^2 \phi_o'' \delta t_{\text{in}}. \quad (2)$$

When the three dispersive elements satisfy the lens-equation [27]

$$-\frac{1}{\phi_l''} = \frac{1}{\phi_i''} + \frac{1}{\phi_o''}, \quad (3)$$

the output is a temporally magnified image of the input with magnification  $M = \frac{\delta t_{\text{out}}}{\delta t_{\text{in}}} = -\frac{\phi_o''}{\phi_i''}$ . The negative magnification

implies that the time-lens creates temporally inverted image of the input photons. Note that a narrowband filter or a dispersive element do not have the same effect on the temporal wavefunction as the time-lens because they stretch each photon in time, without affecting the delay between the centers.

Our experiment was designed to achieve a magnification of  $\approx 9.8x$ . The initial GDD was introduced by 15 km spool of SMF-28 fiber with  $\phi_i'' = -326 \text{ ps}^2$ . The negative sign indicates that the dispersion is anomalous and results in a negative chirp with higher frequencies travelling faster than the lower ones. A large output GDD  $\phi_o'' = -3190 \text{ ps}^2$  corresponding to 150 km of SMF-28 was achieved by using a chirped Bragg grating (CBG) centered at 1550.92 nm. The EOM was driven by a rf signal with frequency  $\nu_m = \frac{\omega_m}{2\pi} = 2.786 \text{ GHz}$  and was locked to the Ti-Sapphire laser. The  $\pi$ -phase-shift voltage  $V_\pi$  of the modulator was measured to be 3.49(6) V, at 2.786 GHz (see S.I.). The rf signal amplitude  $V_m$  was set to 12.3 V so that the group delay dispersion introduced by the EOM  $\phi_l'' \approx 296 \text{ ps}^2$  (see S.I.) and satisfies the time-lens equation (3). Note that the GDD introduced by the lens is normal (positive) whereas that of input and output fibers is anomalous (negative). With these conditions, the lens is a converging lens [27].

To demonstrate the working and resolving power of our time-lens, we first inject two photons into the lens, one arriving in early time-bin  $t_e$  and the other arriving in late time-bin  $t_l$ . The delay between the two time bins  $\delta t_{\text{in}} = t_l - t_e$  is tunable and is chosen to be 20 - 60 ps, smaller than the timing jitter ( $\approx 100 \text{ ps}$ ) of the detector so that the two photons cannot be directly resolved. The individual photon pulse width was measured using HOM interference as 16.7(7) ps (see S.I.). The two photons are generated using a Type-II, collinear spontaneous parametric down conversion (SPDC) process in a periodically-poled KTP crystal pumped by a pulsed Ti-Sapphire laser (see Fig.1(a) and S.I. for details). The orthogonally polarized photons are separated using a PBS, a relative delay is introduced between them and they are then recombined into a single-mode fiber using a fused-fiber beamsplitter. The photons are subsequently filtered using an in-fiber bandpass filter centered at 1550.92 nm, with a FWHM bandwidth of  $\approx 75 \text{ GHz}$  (0.6 nm) and sent to the time lens. The photons at the output of the time lens are detected using a SNSPD and their arrival time is recorded using a Time Interval Analyzer (TIA).

Fig.2(a) shows the observed photon pulses at the output of the lens for different input delays  $\delta t_{\text{in}}$  between the two photons. We can clearly resolve the two photons with input delay as short as 23 ps, consistent with the estimated time resolution, ratio of the effective focal length to the aperture of the lens,  $\delta t_0 = \frac{2V_\pi}{V_m \omega_m} \approx 30 \text{ ps}$  [27]. Fig.2(b) plots the measured delay between photons at the output of the lens as a function of delay at the input. The linearity of the plot indicates faithful temporal magnification of input photons. The slope of this linear plot is the magnification factor  $M$  and is measured to be 9.6(2), in good agreement with the design value of  $M = 9.8$ . The small discrepancy between the observed and

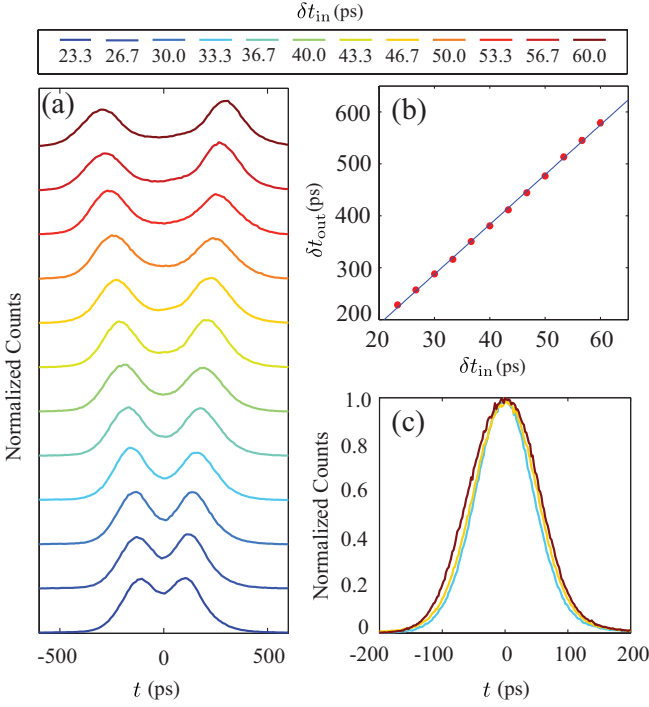


FIG. 2. (a), Observed photon pulses after the time-lens, for different input time delays  $\delta t_{in}$ . The two photons are very well resolved after the time lens for delay as small as  $\approx 23$  ps. (b), Measured delay (red markers) between photons at the output of the lens as a function of delay at the input. The delay increases linearly, with a slope  $M = 9.6(2)$  where the uncertainty is from the linear fit (blue solid line). The size of the errorbars, representing statistical error in finding peaks of photon pulses, is less than the size of markers. (c) Because of the detector jitter ( $\sim 100$  ps) of SNSPD, without the time-lens, the two photons cannot be resolved even for delay  $\delta t_{in}$  as large as 60 ps.

the designed magnification factors is due to marginal overfilling of the time-lens aperture for higher  $\delta t_{in}$  which leads to lower magnification (see S.I.). Furthermore, the measured individual photon pulsewidth (FWHM) at the lens output is 186(1) ps (after correcting for detector jitter). This is again in good agreement with the observed magnification factor, given the input pulse width was estimated to be 16.7(7) ps. For comparison, Fig.2(c) shows the observed TIA response when the photons are incident on the detector without a time-lens. The two photons are completely unresolved by the detector. It clearly demonstrates the advantage offered by a time-lens.

Simple measurements of the time delay between two photons, which are essentially projective measurements of the two-photon temporal wavefunction, do not provide any insight into quantum correlations of the photons. For example, single channel delay measurements cannot distinguish between two-photon states corresponding to temporally bunched and anti-bunched photons [34]. In the bunched state ( $|2_e, 0_l\rangle - |0_e, 2_l\rangle$ ), both the photons arrive in the *early* time-bin or both in the *late* time-bin. In the anti-bunched state ( $|1_e, 1_l\rangle$ ), one photon arrives early and the other late. HOM

interference can be used to reveal bunching/anti-bunching correlations between two photons, but it too cannot differentiate between an entangled state  $|2_e, 0_l\rangle - |0_e, 2_l\rangle$  and correlated states  $|2_e, 0_l\rangle$  or  $|0_e, 2_l\rangle$ , all of which have bunched photons. An alternative is to measure the Joint-temporal intensity (JTI) which can characterize temporal correlations of a two-photon state, analogous to the joint-spectral intensity (JSI) which is used to characterize spectral correlations between photon pairs, for example, those generated using SPDC [35]. JTI is the probability of finding two photons, one at time  $t_1$  and the other at  $t_2$ , and is defined as  $|\psi(t_1, t_2)|^2$  where  $\psi(t_1, t_2)$  is the two-photon temporal wavefunction [36]. JTI of a two-photon state can be easily measured using a beam-splitter and time-resolved coincident detection events at two detectors (see Fig.1(d)). However, direct JTI measurements using single-photon detectors are limited in time-resolution because of the detector jitter. In the following, we demonstrate that a time-lens expands the two-photon temporal wavefunction and also preserves the quantum correlations of the wavefunction. This magnification allows us to measure the JTI and hence unravel correlations of two-photon states with a resolution beyond the limitations imposed by detector jitter. Note that a JTI measurement cannot determine entanglement of photons because it is oblivious to their relative phase. However, similar time-resolved detection (and associated reduction of the effective detection jitter) is required to determine entanglement [37, 38].

To generate two-photon states with bunched and anti-bunched temporal correlations, we use a combination of a HWP, a PBS (see S.I.) and a delay line. Following ref.[39, 40] and as shown in S.I., when the HWP is set an angle  $\theta = 22.5^\circ$  with respect to the horizontal and the JSI of the two-photon wavefunction is symmetric under exchange of signal and idler, the two-photon state entering the time-lens is

$$|\Psi_B\rangle = \int \int dt_1 dt_2 \psi(t_1, t_2) [a^\dagger(t_1 - t_e) a^\dagger(t_2 - t_e) - a^\dagger(t_1 - t_l) a^\dagger(t_2 - t_l)] |0\rangle \quad (4)$$

where  $a^\dagger(t - t_{e(l)})$  is the photon creation operator corresponding to the *early* (*late*) time-bin. This is a time-bin entangled two-photon state where the two photons are always bunched, either appearing in the *early* time-bin ( $t_e$ ) or in the *late* time-bin ( $t_l$ ). Fig.3(a) shows the simulated JTI for this state, with the individual photon pulses assumed to be gaussian (see S.I.). Note that there is a propagation phase associated with the second term in (4) because of the differential delay but our experiment measures JTI which is not affected by this phase. When the HWP angle  $\theta = 0$ , the two-photon state at the input of the lens is

$$|\Psi_{AB}\rangle = \int \int dt_1 dt_2 \psi(t_1, t_2) a^\dagger(t_1 - t_e) a^\dagger(t_2 - t_l) |0\rangle. \quad (5)$$

Now, the two photons always arrive in different time-bins. Note that this state is not time-bin entangled but the beamsplitter used for JTI measurement after the lens cannot distinguish

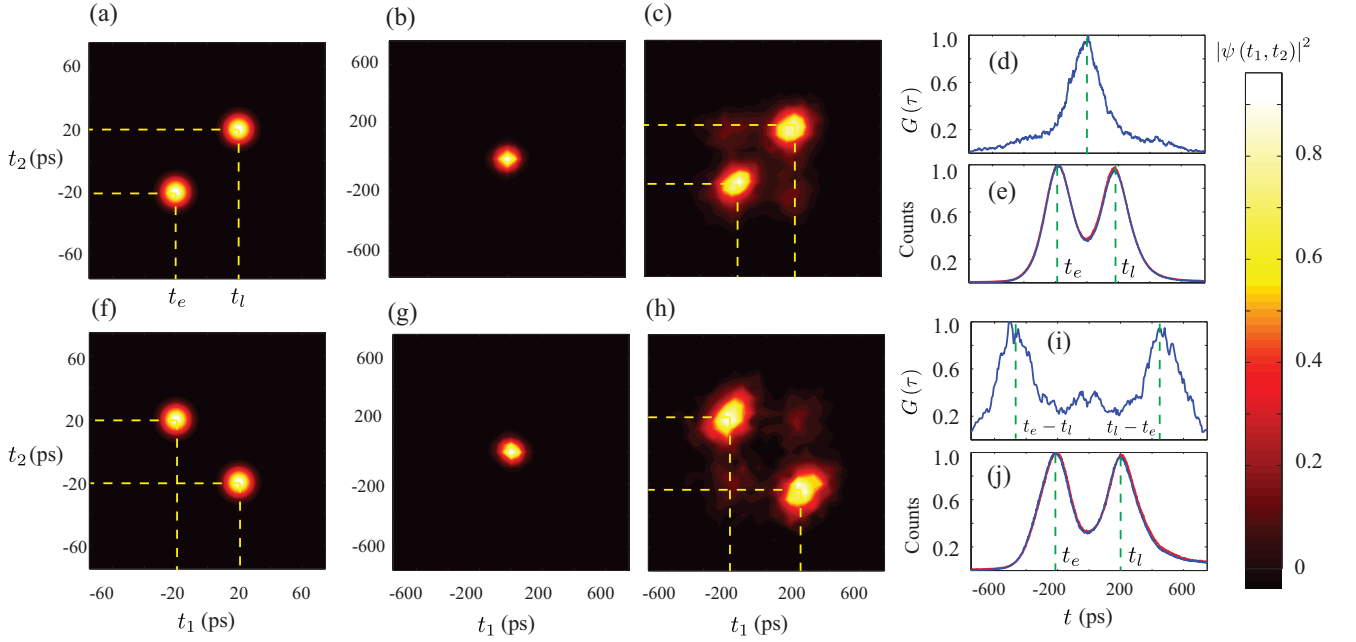


FIG. 3. (a), Simulated JTI of the bunched two-photons state before the time-lens. (b), Measured JTI using setup shown in Fig.1(d), without the time-lens. The temporal correlations cannot be resolved at all. (c), Measured JTI with the time-lens. The two photons can now be very clearly resolved, showing bunched behavior. The measured delay between the two photons is  $\approx 360$  ps when the input delay  $\delta t_{\text{in}}$  was set at 40 ps. (d) Measured  $G(\tau)$ , the probability of finding two photons with time difference  $\tau$ .  $G(\tau)$  peaks at  $\tau = 0$ , consistent with bunched behavior. (e) Measured singles counts on two detectors. (f)-(j) Corresponding results for the anti-bunched state.  $G(\tau)$  now peaks at  $\tau = \pm(t_e - t_l) \approx 420$  ps, showing anti-bunched photons. Note that the single channel measurements of photon pulses cannot distinguish between the two states.

between the two photons and therefore, induces entanglement (see S.I.). The simulated JTI for this anti-bunched state is shown in Fig.3(f).

Fig.3(b,c) show the measured JTI for the bunched state  $|\Psi_B\rangle$ , without and with a time-lens, respectively. In the absence of time-lens, direct measurement of JTI (using setup shown in Fig.1(d)) cannot resolve any correlations in the two-photons state because the time-bins are separated by a delay (40 ps) less than the timing jitter ( $\approx 106$  ps) of the two detectors. By using a time-lens, we magnify the temporal correlations between the photons which are now easily resolved by JTI measurements (Fig.3(c)). A good agreement of the measured JTI with the simulated JTI shows that the time-lens faithfully magnifies the two-photon wavefunction and also preserves its temporal correlations. A small probability of photons arriving in different time bins (anti-bunched, along the anti-diagonal) is also observed in this plot. This is mainly because of multi-photon processes in the SPDC (see S.I.). The measured delay between the time-bins  $\delta t \approx 360$  ps is consistent with the observed magnification.

To further quantify this behavior, in Fig.3(d) we plot the probability  $G(\tau)$  of photons arriving with a time difference  $\tau$ , i.e.,

$$G(\tau) = \int \int dt_1 dt_2 |\Psi(t_1, t_2)|^2 \delta(\tau - t_1 + t_2). \quad (6)$$

As can be seen,  $G(\tau)$  peaks at  $\tau = 0$  again verifying that the photons are bunched.

Fig.3(f-j) show the corresponding results for the anti-bunched state  $|\Psi_{AB}\rangle$ . Again, without the time-lens no correlations are observed in the JTI whereas with the time-lens we clearly see that the two photons always arrive in different time-bins. The probability  $G(\tau)$  now peaks at  $\tau \approx t_l - t_e$ . Also, a finite probability of bunching (along the diagonal) is observed which is due to multi-photon processes in the SPDC (see S.I.). To further highlight the significance of JTI measurements, in Fig.3(e) and (j), we plot the observed singles count on the two detectors, for bunched and anti-bunched cases, respectively. The plots for the two states are exactly identical, have no information about their correlations and the peaks merely show the high probability of detecting a photon. This confirms that single channel delay measurements, in general, cannot be used to characterize two-photon states.

Finally, we show that a time-lens also maps temporal correlations of input photons to frequency correlations of outgoing photons. As shown in (1), the EOM introduces a frequency shift  $\delta\nu$  between two photons separated by a temporal delay  $\delta t_{\text{in}}$  at its input. The CBG used after the EOM maps this frequency shift to time which is then measured using the TIA. Because this frequency-to-time mapping is linear, the time-axis in Fig.3(c,h) could be easily rescaled to frequency using (2) and shows that the two-photon wavefunction at the lens output is also frequency-bin entangled. Note that for frequency-to-time mapped spectral measurements at the lens output, the GDD of the CBG need not satisfy the lens equation [14, 31]. However, in that case, the output of the CBG is

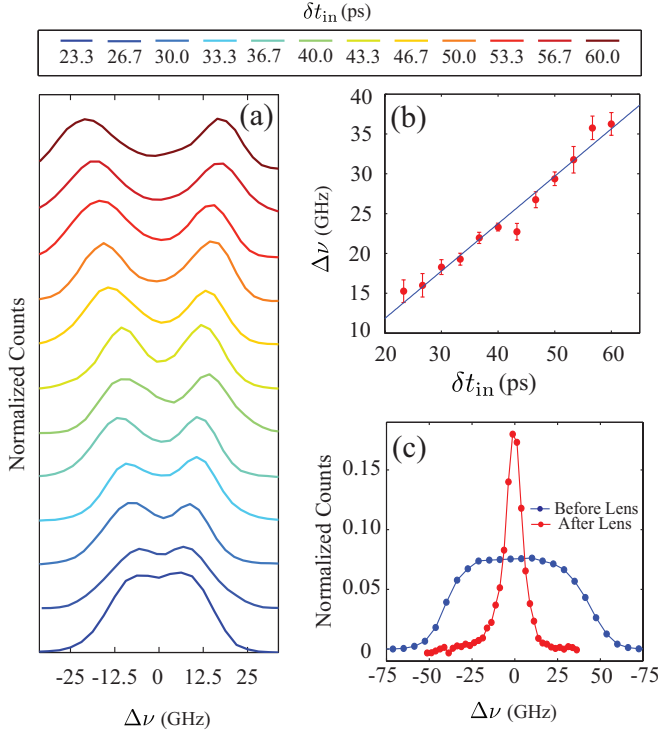


FIG. 4. (a), Measured spectrum of the photon pulses, for different input delay  $\delta t_{in}$ . (b), Relative frequency shift as a function of input delay  $\delta t_{in}$ . A linear fit (blue line) to the measured data (red markers) gives a slope of 0.60(8) and agrees well with slope of 0.54 estimated using (1). (c), Measured spectral profile before the time-lens (FWHM  $\sim 75$  GHz) and after the time-lens (FWHM  $\sim 9$  GHz, corrected for monochromator bandwidth of 8.2GHz) gives a spectral compression factor of  $\approx 8.3\times$ .

not a temporally magnified image of the input, i.e., while the first part of (2) holds, the second does not. Choosing a CBG with a GDD fulfilling the lens equation, as we have done here, allows for simultaneous spectral and temporal measurements. To further verify this frequency shift, we used a monochromator to independently measure the spectrum of photons at the lens output. Fig.4(a) shows the measured spectrum for different input delays  $\delta t$  and Fig.4(b) plots the frequency shift as a function of delay  $\delta t$ . As expected, frequency shift increases linearly with a slope 0.60(8) which compares well with the slope 0.54 estimated using (1). We also confirmed spectral compression of single photons and Fig.4(c) plots the measured single-photon marginal spectrum before and after the time-lens. The measured bandwidth is  $\approx 75$  GHz before the lens and 9(1) GHz after the lens, corresponding to a spectral compression of  $\approx 8.3\times$ .

We have shown 9.6x temporal magnification of a two-photon temporal wavefunction using a deterministic, electro-optic modulator based time-lens. In this demonstration, the time-lens was driven at only 2.8 GHz whereas commercially available EOMs can easily achieve 40 GHz operation. By using higher rf frequencies, this technique could easily be adapted to achieve much higher magnification and thereby re-

solve sub-picosecond time correlations using existing single-photon detectors. Furthermore, by using an arbitrary waveform generator to drive the EOM, this technique could be used to reshape single or multi-photons, for example, a gaussian wavepacket could be transformed to an exponentially decaying or rising wavepacket to match the emission profile of a photonic or an atomic cavity.

#### Acknowledgements

This research was supported by AFOSR-MURI FA9550-14-1-0267, ONR, Sloan Foundation and the Physics Frontier Center at the Joint Quantum Institute. We thank T. Huber, J. Fan and G. Solomon for fruitful discussions, Q. Quraishi for kindly providing the nanowire detectors, A. Migdall and S. Polyakov for providing the HydraHarp time tagging module and J. Bienfang for the high power amplifier.

- 
- [1] N. Gisin and R. Thew, Nat. Photon. **1**, 165 (2007).
  - [2] J.-W. Pan, Z.-B. Chen, C.-Y. Lu, H. Weinfurter, A. Zeilinger, and M. Żukowski, Rev. Mod. Phys. **84**, 777 (2012).
  - [3] J. Brendel, N. Gisin, W. Tittel, and H. Zbinden, Phys. Rev. Lett. **82**, 2594 (1999).
  - [4] M. Sasaki and et. al., Opt. Express **19**, 10387 (2011).
  - [5] A. P. Vandevender and P. G. Kwiat, J. Mod. Opt. **51**, 1433 (2004).
  - [6] S. Tanzilli and et. al., Nature **437**, 116 (2005).
  - [7] P. Kolchin, C. Belthangady, S. Du, G. Y. Yin, and S. E. Harris, Phys. Rev. Lett. **101**, 103601 (2008).
  - [8] O. D. Odele and et.al., Opt. Express **23**, 21857 (2015).
  - [9] N. Matsuda, Science Advances **2** (2016).
  - [10] M. Allgaier and et.al., Nat. Commun. **8**, 14288 (2017).
  - [11] L. J. Wright, M. Karpiński, C. Söller, and B. J. Smith, Phys. Rev. Lett. **118**, 023601 (2017).
  - [12] H. J. Kimble, Nature **453**, 1023 (2008).
  - [13] J. Lavoie, J. M. Donohue, L. G. Wright, A. Fedrizzi, and K. J. Resch, Nat. Photon. **7**, 363 (2013).
  - [14] M. Karpiński, M. Jachura, L. J. Wright, and B. J. Smith, Nat. Photon. **11**, 53 (2016).
  - [15] A. Aspuru-Guzik and P. Walther, Nat Phys **8**, 285 (2012).
  - [16] I. Carusotto and C. Ciuti, Rev. Mod. Phys. **85**, 299 (2013).
  - [17] M. J. Hartmann, Journal of Optics **18**, 104005 (2016).
  - [18] C. Noh and D. G. Angelakis, Reports on Progress in Physics **80**, 016401 (2017).
  - [19] K. R. Motes, A. Gilchrist, J. P. Dowling, and P. P. Rohde, Phys. Rev. Lett. **113**, 120501 (2014).
  - [20] Y. He and et. al., arXiv **1603.04127** (2016).
  - [21] M. Pant and D. Englund, Phys. Rev. A **93**, 043803 (2016).
  - [22] A. Schreiber and et. al., Science **336**, 55 (2012).
  - [23] S. Mittal, V. V. Orre, and M. Hafezi, Opt. Express **24**, 15631 (2016).
  - [24] F. Marsili and et. al., Nat Photon **7**, 210 (2013).
  - [25] C. M. Natarajan, M. G. Tanner, and R. H. Hadfield, Supercond. Sci. Technol. **25**, 063001 (2012).
  - [26] N. Calandri, Q.-Y. Zhao, D. Zhu, A. Dane, and K. K. Berggren, Appl. Phys. Lett. **109**, 152601 (2016).
  - [27] B. H. Kolner, IEEE J. Quant. Electron. **30**, 1951 (1994).
  - [28] C. V. Bennett and B. H. Kolner, Opt. Lett. **24**, 783 (1999).
  - [29] M. A. Foster and et.al., Nature **456**, 81 (2008).
  - [30] M. A. Foster and et.al., Nat. Photon. **3**, 581 (2009).



- [31] J. M. Donohue, M. Mastrovich, and K. J. Resch, Physical Review Letters **117**, 243602 (2016).
- [32] J. M. Donohue, M. Agnew, J. Lavoie, and K. J. Resch, Phys. Rev. Lett. **111**, 153602 (2013).
- [33] S. Ramelow, L. Ratschbacher, A. Fedrizzi, N. K. Langford, and A. Zeilinger, Phys. Rev. Lett. **103**, 253601 (2009).
- [34] W. Tittel, J. Brendel, H. Zbinden, and N. Gisin, Phys. Rev. Lett. **81**, 3563 (1998).
- [35] G. Harder and et.al., Opt. Express **21**, 13975 (2013).
- [36] O. Kuzucu, F. N. C. Wong, S. Kurimura, and S. Tovstonog, Phys. Rev. Lett. **101**, 153602 (2008).
- [37] J. D. Franson, Phys. Rev. Lett. **62**, 2205 (1989).
- [38] P. G. Kwiat, A. M. Steinberg, and R. Y. Chiao, Phys. Rev. A **47**, R2472 (1993).
- [39] P. S. Kuo, T. Gerrits, V. B. Verma, and S. W. Nam, Opt. Lett. **41**, 5074 (2016).
- [40] T. Gerrits and et.al., Phys. Rev. A **91**, 013830 (2015).

# Supplementary Information: Temporal and Spectral Manipulations of Correlated Photons

Sunil Mittal,<sup>1,2</sup> Venkata Vikram Orre,<sup>1,2</sup> Alessandro Restelli,<sup>1</sup> Reza Salem,<sup>3</sup> Elizabeth A. Goldschmidt,<sup>4,1</sup> and Mohammad Hafezi<sup>1,2</sup>

<sup>1</sup>*Joint Quantum Institute, NIST/University of Maryland, College Park, MD 20742, USA*

<sup>2</sup>*Department of Electrical and Computer Engineering, and IREAP, University of Maryland, College Park, MD 20742, USA*

<sup>3</sup>*PicoLuz, LLC, Jessup, MD 20794, USA*

<sup>4</sup>*U.S. Army Research Laboratory, Adelphi, MD 20783, USA*

## 1. ACTION OF A TIME-LENS ON TWO-PHOTON WAVEFUNCTION

In this section, we derive the relations governing action of a time-lens on a two-photon wavefunction. We start with a general two-photon state at the input of the lens

$$|\Psi\rangle = \int \int dt_1 dt_2 \psi(t_1, t_2) a^\dagger(t_1) a^\dagger(t_2) |0\rangle, \quad (S1)$$

where  $\psi_{\text{in}}(t_1, t_2)$  is the two-photon temporal wavefunction. Using 2D Fourier transform, the temporal wavefunction could be written in frequency domain as

$$\psi_{\text{in}}(t_1, t_2) = \frac{1}{2\pi} \int \int d\omega_1 d\omega_2 \exp(i\omega_1 t_1) \exp(i\omega_2 t_2) \tilde{\psi}_{\text{in}}(\omega_1, \omega_2), \quad (S2)$$

where  $\tilde{\psi}_{\text{in}}(\omega_1, \omega_2)$  is now the spectral two-photon wavefunction at the input.

The input dispersion element introduces a group delay dispersion (GDD)  $\phi_i'' = \frac{d^2 \phi_i(\omega)}{d\omega^2}$  where  $\phi_i(\omega)$  is the frequency dependent phase. This dispersion results in a chirped temporal wavefunction ( $\psi_{\text{ch}}(t_1, t_2)$ ) given as

$$\psi_{\text{ch}}(t_1, t_2) = \frac{1}{2\pi} \int \int d\omega_1 d\omega_2 \exp(i\omega_1 t_1) \exp(i\omega_2 t_2) \exp\left(-i\phi_i'' \frac{(\omega_1 - \omega_0)^2}{2}\right) \exp\left(-i\phi_i'' \frac{(\omega_2 - \omega_0)^2}{2}\right) \tilde{\psi}_{\text{in}}(\omega_1, \omega_2). \quad (S3)$$

Here  $\omega_0$  is the central frequency of the spectral wavefunction.

After the input dispersion, the two-photon wavefunction is subjected to the time-lens. Here, we used an electro-optic phase modulator (EOM) based time-lens. The EOM adds a time-dependent phase to the dispersed wavefunction. Specifically, the phase introduced by the EOM is  $\phi_l(t) = -\frac{\pi V_m}{V_\pi} \cos(\omega_m t)$ , where  $V_m, V_\pi$  are the amplitude of the applied rf field and the  $\pi$ -phase shift voltage of the EOM, respectively [1]. For  $\omega_m t \ll 1$ ,  $\phi_l(t) \simeq \frac{\pi V_m}{2V_\pi} \omega_m^2 t^2$ , i.e., the phase-shift varies quadratically in time as is required for a time-lens. This time dependent phase also produces a linear frequency shift  $\delta\nu(t) = \frac{1}{2\pi} \frac{d\phi_l}{dt} = \frac{V_m}{2V_\pi} \omega_m^2 t$ . This linear frequency chirp is opposite to the chirp introduced by the input dispersion and therefore, leads to bandwidth compression. The temporal two-photon wavefunction after the EOM, with time-dependent phase shift is given as

$$\psi_{\text{EOM}}(t_1, t_2) = \exp\left(i\frac{\pi V_m}{2V_\pi} \omega_m^2 t_1^2\right) \exp\left(i\frac{\pi V_m}{2V_\pi} \omega_m^2 t_2^2\right) \psi_{\text{ch}}(t_1, t_2). \quad (S4)$$

The spectral two-photon function after the EOM can be obtained using Fourier transform of (S4) as

$$\tilde{\psi}_{\text{EOM}}(\omega_1, \omega_2) = \int \int dt_1 dt_2 \exp(-i\omega_1 t_1) \exp(-i\omega_2 t_2) \psi_{\text{EOM}}(t_1, t_2) \quad (S5)$$

Finally, the temporal wavefunction after the GDD introduced by the output dispersion  $\phi_o''$  is

$$\psi_{\text{out}}(t_1, t_2) = \frac{1}{2\pi} \int \int d\omega_1 d\omega_2 \exp(i\omega_1 t_1) \exp(i\omega_2 t_2) \exp\left(-i\phi_o'' \frac{(\omega_1 - \omega_0)^2}{2}\right) \exp\left(-i\phi_o'' \frac{(\omega_2 - \omega_0)^2}{2}\right) \tilde{\psi}_{\text{EOM}}(\omega_1, \omega_2). \quad (S6)$$

Using above equations, the temporal wavefunction at the output of the lens can be easily calculated for any general two-photon wavefunction at its input. Here we show numerically simulated results for a time-bin entangled two-photon state incident on the

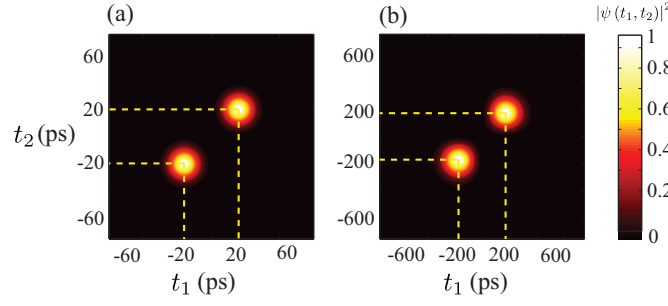


FIG. S1. **a**, Simulated JTI for a time-bin entangled state with bunched photons and  $\delta t_{\text{in}} = t_l - t_e = 40$  ps. **b**, Simulated JTI after the time-lens. The lens has magnified the two-photon wavefunction by a factor of  $\approx 10\times$ .

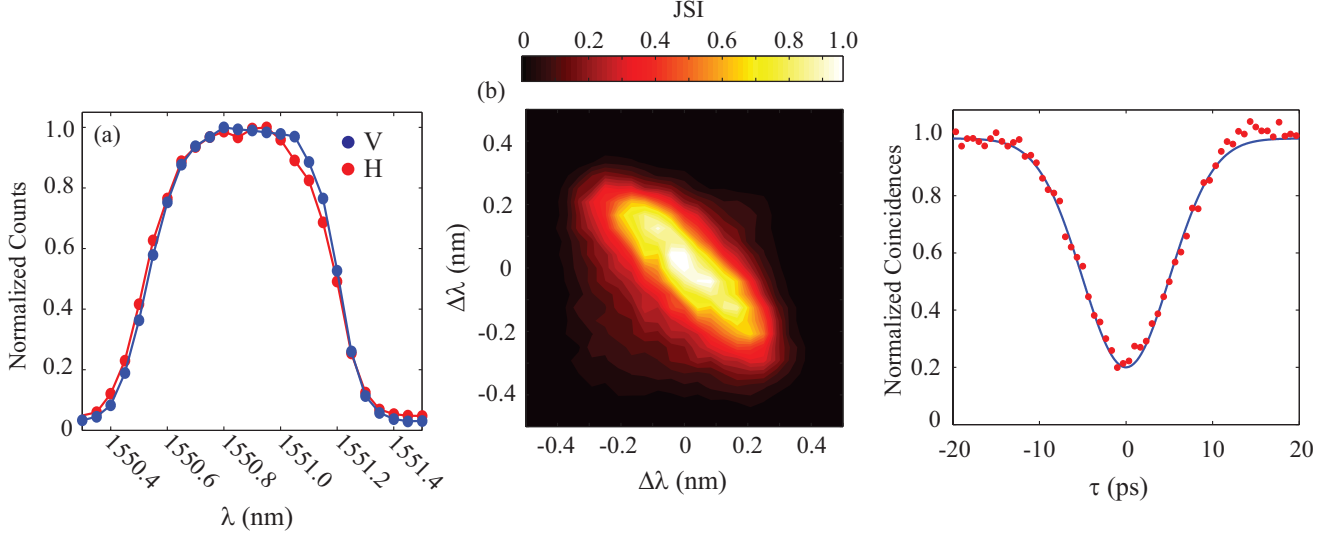


FIG. S2. **a**, Measured marginal spectra of  $H$  and  $V$  polarized photons generated using Type-II SPDC and subsequently filtered using a bandpass DWDM filter with FWHM bandwidth  $\approx 0.6$  nm. **b**, Measured JSI after the DWDM filter. The JSI is nearly symmetric as is required for generation of time-bin entangled photons using HWP and a PBS. **c**, Measured HOM interference visibility of  $\approx 80\%$  shows good indistinguishability of photons.

time-lens. The input two-photon wavefunction in this case is written as

$$\psi_{\text{in}}(t_1, t_2) = \exp\left(-\frac{(t_1 - t_e)^2}{2\sigma_T^2}\right) \exp\left(-\frac{(t_2 - t_e)^2}{2\sigma_T^2}\right) + \exp\left(-\frac{(t_1 - t_l)^2}{2\sigma_T^2}\right) \exp\left(-\frac{(t_2 - t_l)^2}{2\sigma_T^2}\right), \quad (\text{S7})$$

where  $t_e, t_l$  are the times corresponding to the early and the late time-bins.  $\sigma_T$  is the single-photon pulsewidth. This wavefunction represents a bunched state where both the photons arrive either in the *early* or the *late* time-bin. Fig.S1(a) shows the simulated JTI, i.e.,  $|\psi(t_1, t_2)|^2$  at the input and its magnified image at the output of the time lens. Here  $\sigma_T = 10$  ps,  $\delta t = t_l - t_e = 40$  ps and the lens parameters are same as mentioned in the main text. Clearly, the time-lens magnifies the two-photon temporal wavefunction and because it is a linear transformation, it also preserves photonic correlations.

## 2. SPDC SOURCE CHARACTERIZATION

We used a collinear Type-II SPDC process to generate the time-bin entangled two-photon states. A 30 mm long periodically-poled KTP (KTiOPO<sub>4</sub>) crystal was pumped with a pulsed Ti-Sapphire laser emitting  $\approx 10$  ps pulses at  $\approx 775.45$  nm wavelength. The crystal had a poling period of  $46.2 \mu\text{m}$  and was phase-matched to produce nearly degenerate, orthogonally polarized ( $H$  and  $V$ ) signal and idler photons near  $1550.9$  nm, at  $30^\circ\text{C}$ . The output of SPDC was first collimated and collected in a polarization maintaining (PM) single-mode fiber. This ensures that the collected photon pairs are from a single spatial mode. The



output of the fiber was then re-collimated into free space and fed to a combination of a HWP and a PBS. This combinations works as a variable beam splitter and as explained later, was used to generate the bunched or anti-bunched time-bin entangled photons [2, 3]. A differential delay was introduced in the two arms of the PBS using a delay line. This differential delay  $\delta t_{\text{in}} = t_l - t_e$ , i.e., the delay between the two time bins. To eliminate any artifacts arising from polarization dependent loss and dispersion, another HWP was used in the  $V$  polarization arm of the PBS and it was rotated to  $H$ . Therefore, both the photons entering the lens had identical polarization, wavelength and spatial mode. Photons in both arms of the PBS were then individually recollimated into PM fibers and then recombined using a fused-fiber PM beamsplitter. The output (one port) of the beamsplitter was then filtered using an in-fiber bandpass filter, with a FWHM of  $\approx 0.6$  nm. This spectral filtering improves the spectral indistinguishability of the photons. Finally, this filtered output was input of the lens, via a fiber polarization controller. Note that if the two photons have different central wavelengths, they will experience a differential delay in the input and the output dispersive elements (fiber spool and CBG, respectively) and the lens output will not be a temporally magnified image of the input.

Fig.S2(a) shows the measured marginal spectra of the  $H$  and  $V$  polarized photons and they overlap very well. However, as we will explain in the following, generation of time-bin entangled photons using a combination of HWP and PBS requires the joint-spectral amplitude of the two-photon wavefunction to be symmetric, i.e.,  $\tilde{\psi}(\omega_1, \omega_2) = \tilde{\psi}(\omega_2, \omega_1)$ . Therefore, we also measured the JSI  $|\tilde{\psi}|^2$  of the two-photon wavefunction using chirped Bragg grating as a frequency-to-time converter and recording coincidences in TIA [3]. The observed JSI is shown in Fig.S2(b). Although the two-photon spectral wavefunction (before entangling) is not completely factorizable, it is nearly symmetric with respect to the diagonal and therefore satisfies the requirement for generating time-bin entangled photons. A symmetric JSA also leads a high visibility HOM interference [4]. We confirmed this and the result is shown in Fig.S2(c). We measure a HOM interference visibility of  $\approx 80\%$ . Also, using the width of the HOM interference, the single-photon temporal pulsewidth is estimated to be 16.7(7) ps.

### 3. GENERATION OF TIME-BIN ENTANGLED TWO-PHOTON STATES

In this section we discuss the formalism to generate of time-bin entangled photons using a combination of a HWP, a PBS and a delay line, as mentioned above. We start with writing the two-photon state just after the SPDC as

$$\begin{aligned} |\Psi\rangle &= \int \int d\omega_1 d\omega_2 \tilde{\psi}(\omega_1, \omega_2) a_H^\dagger(\omega_1) a_V^\dagger(\omega_2) |0\rangle \\ &= \int \int dt_1 dt_2 \psi(t_1, t_2) a_H^\dagger(t_1) a_V^\dagger(t_2) |0\rangle. \end{aligned} \quad (\text{S8})$$

The temporal  $(\psi(t_1, t_2))$  and spectral two-photon wavefunctions  $(\tilde{\psi}(\omega_1, \omega_2))$  are related by 2D Fourier transform (S2).

Following SPDC, the two photons are subjected to a variable beamsplitter implemented using a HWP and a PBS. We first analyze the case when the HWP is oriented at an angle  $\theta = 22.5^\circ$  with respect to the horizontal axis and results in a time-bin entangled state where the photons are always bunched (see (4) of main text). The HWP rotates the polarizations of the two photons such that the two-photon state is now

$$|\Psi\rangle = \int \int d\omega_1 d\omega_2 \tilde{\psi}(\omega_1, \omega_2) a_D^\dagger(\omega_1) a_A^\dagger(\omega_2) |0\rangle, \quad (\text{S9})$$

where  $a_D^\dagger = \frac{1}{\sqrt{2}}(a_H^\dagger + a_V^\dagger)$  and  $a_A^\dagger = \frac{1}{\sqrt{2}}(a_H^\dagger - a_V^\dagger)$  are the photon creation operators for diagonal ( $D$ ) and anti-diagonal ( $A$ ) basis, respectively. Rewriting this state in the  $H$  and  $V$  basis gives

$$|\Psi\rangle = \int \int d\omega_1 d\omega_2 \tilde{\psi}(\omega_1, \omega_2) [a_H^\dagger(\omega_1) a_H^\dagger(\omega_2) - a_V^\dagger(\omega_1) a_V^\dagger(\omega_2) + a_V^\dagger(\omega_1) a_H^\dagger(\omega_2) - a_H^\dagger(\omega_1) a_V^\dagger(\omega_2)] |0\rangle. \quad (\text{S10})$$

When the JSI of the SPDC process is symmetric, i.e.,  $\tilde{\psi}(\omega_1, \omega_2) = \tilde{\psi}(\omega_2, \omega_1)$ , the last two terms in the above expression cancel each other and the two-photon state is simply [2, 3]

$$|\Psi\rangle = \int \int d\omega_1 d\omega_2 \tilde{\psi}(\omega_1, \omega_2) [a_H^\dagger(\omega_1) a_H^\dagger(\omega_2) - a_V^\dagger(\omega_1) a_V^\dagger(\omega_2)] |0\rangle. \quad (\text{S11})$$

This is a polarization entangled state of two-photons where both the photons are either  $H$  polarized or  $V$  polarized. This phenomenon is similar to the usual HOM interference with a beamsplitter where both the photons at the output of the beamsplitter

go into same port [2, 3]. Here, the two polarization modes  $H$  and  $V$  are analogous to the two spatial modes, and the HWP at angle  $\theta = 22.5^\circ$  acts as a 50 : 50 beam splitter.

Then, we use a PBS to spatially separate the  $H$  and  $V$  polarized photons and convert these polarization entangled photons to time-bin entangled photons. The  $H$  and  $V$  polarized photon pairs emerge from different output ports of the PBS and therefore, we can introduce a relative delay  $\delta t$  between. We advance  $H$  polarized photons with respect to  $V$  polarized photons. Both the photons are now either in the early time-bin  $t_e$  associated with  $H$  polarization or in the late time-bin  $t_l$  associated with  $V$  polarization and  $t_l - t_e = \delta t$ . Finally, we use another HWP to rotate  $V$  polarized photons to  $H$ , collect photons from both the paths in two PM single-mode fibers and recombine them using a fused-fiber beamsplitter. The two-photon state after the fiber beamsplitter is

$$\begin{aligned} |\Psi\rangle &= \int \int d\omega_1 d\omega_2 \tilde{\psi}(\omega_1, \omega_2) [\exp(-i\omega_1 t_e) \exp(-i\omega_2 t_e) a^\dagger(\omega_1) a^\dagger(\omega_2) - \exp(-i\omega_1 t_l) \exp(-i\omega_2 t_l) a^\dagger(\omega_1) a^\dagger(\omega_2)] |0\rangle \\ &= \int \int dt_1 dt_2 \psi(t_1, t_2; t_e, t_l) [a^\dagger(t_1 - t_e) a^\dagger(t_2 - t_e) - a^\dagger(t_1 - t_l) a^\dagger(t_2 - t_l)] |0\rangle. \end{aligned} \quad (\text{S12})$$

This is a time-bin entangled two-photon state where the photons always arrive bunched, either at time  $t_e$  or at time  $t_l$ . We have dropped polarization indices in this state because now both the photons are always  $H$  polarized. The JTI for this state is shown in Fig.3(a) of the main text.

Next we analyze the case when the HWP angle  $\theta = 0$ , i.e., its axis is aligned with the horizontal and leads to generation of anti-bunched two-photon state (eq. (5) of main text). With this setting, the HWP does not rotate polarizations of the two photons generated by SPDC. It imprints an overall  $\pi$  phase on the two-photon wavefunction which is inconsequential. After the PBS, the two-photon state is same as that generated by the SPDC, i.e.,

$$|\Psi\rangle = \int \int dt_1 dt_2 \psi(t_1, t_2) a_H^\dagger(t_1) a_V^\dagger(t_2) |0\rangle.$$

As before, PBS spatially separates the  $H$  and  $V$  polarizations and we introduce a relative delay between the two arms such that  $H$  polarization corresponds to the early time-bin  $t_e$  and  $V$  to the late time-bin  $t_l$ . We rotate the  $V$  polarization to  $H$  using a HWP, collect them in two single-mode fibers and combine them using a fused-fiber beamsplitter. Therefore, the two-photon state incident on the time-lens is

$$|\Psi\rangle = \int \int dt_1 dt_2 \psi(t_1 - t_e, t_2 - t_l) a^\dagger(t_1 - t_e) a^\dagger(t_2 - t_l) |0\rangle.$$

Note that this state is not a time-bin entangled state. It is simply a correlated, separable state of two photons where one comes early and the other late. But for JTI measurements, we use another fiber beamsplitter after the time-lens. The two output ports of the beamsplitter are connected to single photon detectors each. The two-photon state after the beamsplitters is given as

$$|\Psi\rangle = \int \int dt_1 dt_2 \psi(t_1 - t_e, t_2 - t_l) \left( d_1^\dagger(t_1 - t_e) - i d_2^\dagger(t_1 - t_e) \right) \left( d_1^\dagger(t_2 - t_l) - i d_2^\dagger(t_2 - t_l) \right) |0\rangle. \quad (\text{S13})$$

where  $d_{1,2}^\dagger$  are the photon creation operators on detectors 1 and 2. A measurement of the coincident events on two detectors then projects this state to

$$|\Psi\rangle = \int \int dt_1 dt_2 \psi(t_1 - t_e, t_2 - t_l) \left( d_1^\dagger(t_1 - t_e) d_2^\dagger(t_2 - t_l) + d_2^\dagger(t_1 - t_e) d_1^\dagger(t_2 - t_l) \right) |0\rangle. \quad (\text{S14})$$

This is a measurement induced entangled state where the two photons are always anti-bunched. When detector-1 records an *early* event at time  $t_e$ , detector-2 would record a *late* event at time  $t_l$  and vice-versa. The simulated JTI for this state is shown in Fig.3(f) of the main text.

#### 4. CONTRIBUTION OF MULTI-PHOTON PROCESSES TO MEASURED JTI

In the experimentally measured JTI (Fig.3(c) of main text) we observe some anti-bunched photons at the lens output for ideally bunched photons at the input and vice-versa. These photon pairs showing opposite correlations than expected are because of multi-photon processes in the SPDC. To estimate this contribution, we begin with approximating the multi-photon state after the SPDC as [5]

$$|\Psi\rangle = \sqrt{(1 - p_1 - p_2)} |0_H, 0_V\rangle + \sqrt{p_1} |1_H, 1_V\rangle + \sqrt{p_2} |2_H, 2_V\rangle, \quad (\text{S15})$$

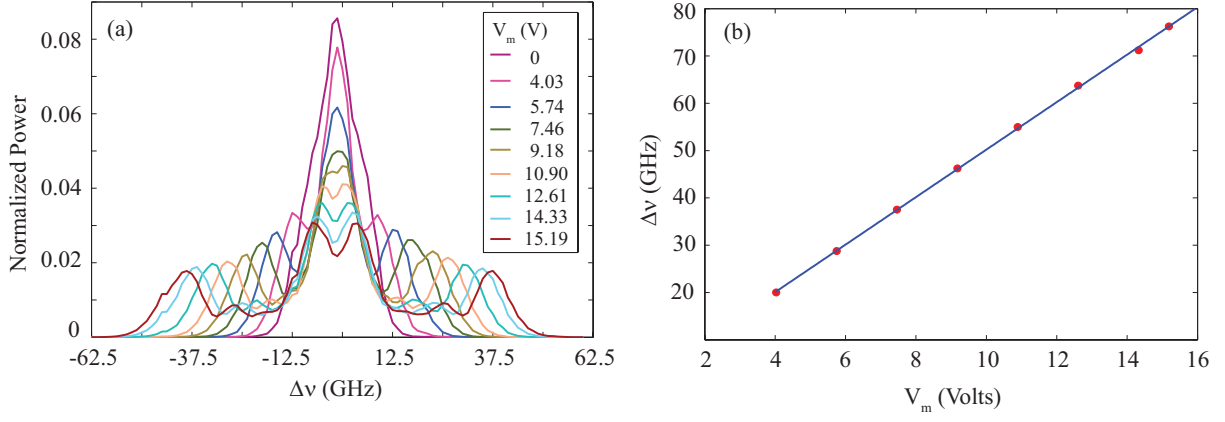


FIG. S3. **a**, Spectral sidebands induced by the phase modulator on CW light, as a function of applied rf amplitude. **b**, Maximum shift as a function of rf amplitude. The slope of the fit gives  $V_\pi = 3.49(6)$  V.

where  $p_1$ ,  $p_2$  are the probabilities per pump pulse to generate one and two photon pairs, respectively. We assume that the probability for generation of more than two photon pairs is negligible. As detailed in the previous sections, these photons are passed through a HWP and a PBS, assigned time-bin  $t_e$  and  $t_l$  corresponding to  $H$  and  $V$  polarizations, respectively, by the delay line and finally recombined using a fiber beamsplitter. For simplicity, we consider the HWP angle  $\theta = 0$  so that the ideal state would be an antibunched state. If the fiber coupling efficiency is  $\eta$ , the multi-photon state in the fiber is

$$|\Psi\rangle \simeq \sqrt{\eta^2 p_1} |1_e, 1_l\rangle + \sqrt{\eta^2 (1-\eta)^2 p_2} [|2_e, 0_l\rangle + |0_e, 2_l\rangle] + \sqrt{2\eta^3 (1-\eta) p_2} [|2_e, 1_l\rangle + |1_e, 2_l\rangle] + \sqrt{\eta^4 p_2} |2_e, 2_l\rangle. \quad (\text{S16})$$

Here, the state  $|2_e, 1_l\rangle$  represents the case when there are two photons in the *early* time-bin and one photon in the *late* time-bin, and so on. Using this relation, we see that the probability of detecting two photons in the *early* or *late* time bins is

$$p(e, e) = p(l, l) = 2 \left( \eta^2 (1-\eta)^2 p_2 + 2\eta^3 (1-\eta) p_2 + \eta^4 p_2 \right) = 2\eta^2 p_2 \quad (\text{S17})$$

and that for detecting one photon each in *early* and *late* time bins is

$$p(e, l) \simeq \eta^2 p_1. \quad (\text{S18})$$

The extra factor of two in eq. (S17) is because of the beamsplitter used for JTI measurements. Therefore, the relative probability of bunched to anti-bunched photons is

$$\frac{p(e, e)}{p(e, l)} = \frac{2p_2}{p_1}. \quad (\text{S19})$$

In our experiment, the SPDC was pumped with 300 mW of power with  $p_1 \approx 0.1$  and  $p_2 = \frac{g_2(0)}{2} p_1^2 \approx 0.009$ , where  $g_2(0) \approx 1.8$  is the second-order intensity correlation function at zero delay. Therefore, the probability of detecting bunched events to anti-bunched events, for an ideally anti-bunched two photon state, is  $\approx 0.2$ . This agrees well with the experimental observation in Fig.3(c) and (h).

## 5. EO PHASE MODULATOR CHARACTERIZATION

The GDD introduced by the EOM is

$$\phi_l'' = \frac{V_\pi}{\pi V_m \omega_m^2}, \quad (\text{S20})$$

where  $V_m$  and  $\omega_m$  are the amplitude and angular frequency of the rf drive field, respectively. To estimate the dispersion of the EOM for a given  $V_m$  and  $\omega_m$ , we need to characterize the  $\pi$  phase-shift voltage  $V_\pi$  of the EOM. We used a CW laser

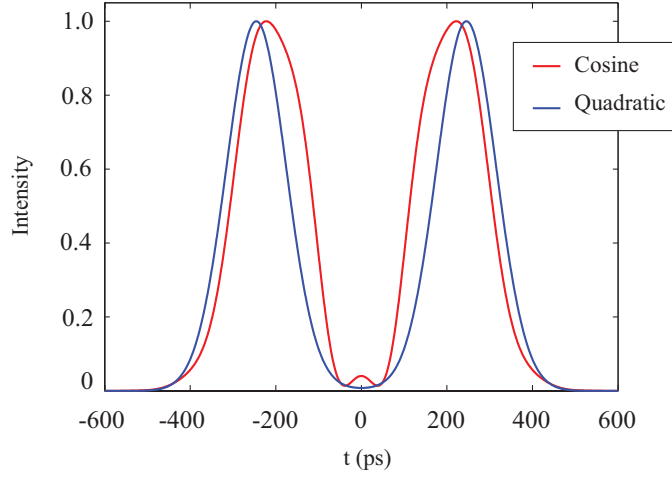


FIG. S4. Simulation results for two photons at the lens output, with quadratic and cosine (EOM) dispersion, with  $\delta t_{\text{in}} = 50$  ps. For higher  $\delta t_{\text{in}}$ , the photons overfill the lens aperture which leads to lower magnification and also some pulse distortions.

to characterize  $V_\pi$ . Consider a CW field  $E = E_o \cos(\omega_0 t)$  propagating through the EOM. The EOM adds a time-dependent phase-shift  $\phi_l(t) = -\frac{\pi V_m}{V_\pi} \cos(\omega_m t)$  to this field. The total phase of the field at the output of the EOM is then

$$\phi = \omega_o t - \frac{\pi V_m}{V_\pi} \cos(\omega_m t). \quad (\text{S21})$$

The time-dependent phase-shift imposed by the EOM also results in a frequency chirp  $\delta\omega(t)$  such that the time varying angular frequency of the field after the EOM is

$$\omega(t) = \frac{d\phi}{dt} = \omega_0 + \frac{\pi V_m}{V_\pi} \omega_m \sin(\omega_m t). \quad (\text{S22})$$

From above relation we see that the maximum shift from the central frequency occurs at  $t = \pm \frac{1}{4} \frac{2\pi}{\omega_m}$ , and therefore, the total shift between the two side-bands is given as

$$\delta\omega_{\text{max}} = \frac{2\pi\omega_m}{V_\pi} V_m. \quad (\text{S23})$$

For a fixed rf drive frequency, the maximum frequency shift is a linear function of  $V_m$  with a slope  $\frac{2\pi\omega_m}{V_\pi}$ . Therefore, a measurement of the maximum shift introduced by the EOM for a given rf drive frequency and amplitude gives the parameter  $V_\pi$  of the EOM.

Fig.S3(a) plots the measured spectrum of the output field for different rf drive amplitudes, for  $\nu_m = 2.786$  GHz. The input to the EOM was CW laser and therefore, the sidebands seen here are because of the EOM. The sidebands move further away from the central frequency as the drive amplitude increases. Also, for no applied drive, the observed spectral width of the CW field is due to the monochromator bandwidth. The observed maximum shift (difference between sidebands) as a function of drive amplitude is shown in Fig.S3(b). As expected, it is a linear plot. A linear fit to the measured data gives a slope of 5.02(8) GHz/V and hence,  $V_\pi = 3.49(6)$  V. In our experiment, the EOM was driven with  $V_m \approx 12.3$  V which gives in a maximum shift of  $\approx 62$  GHz and a dispersion of  $\approx 296$  ps<sup>2</sup>.

## 6. LENS APERTURE AND ABERRATIONS

To achieve a high-fidelity magnified temporal image of the input photons, the dispersion introduced by the time-lens should be quadratic. For an EOM, the time aperture ( $T_a$ ) over which this conditions holds is  $\frac{T_a}{T} < 0.17$  [1], where  $T = \frac{2\pi}{\omega_m}$  is the time-period of the rf field. In our experiment,  $T \approx 360$  ps which implies that  $T_a \approx 61$  ps and for faithful magnification, the total temporal extent of the two photons at the EOM should be less than 60 ps. However, we marginally overfilled the lens aperture for larger values of delay  $\delta t_{\text{in}}$ , given the individual photon pulsewidth was  $\sim 16.7$  ps. For example, with  $\delta t_{\text{in}} = 50$

ps, the measured temporal width, including the two photon pulses and the delay between them, after the 15 km fiber spool was measured to be  $\approx 125$  ps (after correcting for detector jitter). Because of this overfill, the time-varying phase experienced by the photon pulses in EOM is not really quadratic and results in lower magnification. To verify this, in Fig.S4, we show simulation results for magnified two photon pulses at the output of the lens, for an ideal quadratic dispersion and the actual cosine dispersion introduced by EOM. Here, the delay  $\delta t_{\text{in}} = 50$  ps at the input. Comparing the two results, we clearly see that the EOM introduces some pulse distortions because of the overfill. Also, the delay at the output is  $\sim 444$  ps, giving a magnification factor of  $\sim 8.9\times$ . Therefore, aperture overfill also decreases the magnification of the time-lens. These aberrations could be reduced by lowering the rf drive frequency while increasing the drive amplitude so that the EOM dispersion remains same. We were limited in rf drive power and therefore, could not use lower rf frequencies.



- [1] B. H. Kolner, IEEE J. Quant. Electron. **30**, 1951 (1994).
- [2] P. S. Kuo, T. Gerrits, V. B. Verma, and S. W. Nam, Opt. Lett. **41**, 5074 (2016).
- [3] T. Gerrits and et.al., Phys. Rev. A **91**, 013830 (2015).
- [4] G. Harder and et.al., Opt. Express **21**, 13975 (2013).
- [5] D. F. Walls and G. J. Milburn, *Quantum Optics* (Springer-Verlag, Berlin, 2008).